Journal of Power Sources 192 (2009) 544–551

Contents lists available at ScienceDirect

Journal of Power Sources

journal homepage: www.elsevier.com/locate/jpowsour

Assembly pressure and membrane swelling in PEM fuel cells

Y. Zhou, G. Lin, A.J. Shih, S.J. Hu*

Department of Mechanical Engineering, The University of Michigan, Ann Arbor, MI 48109-2125, USA

ARTICLE INFO

Article history:
Received 15 December 2008
Received in revised form 21 January 2009
Accepted 28 January 2009
Available online 7 February 2009

Keywords:
Assembly pressure
Deformation
Current distribution
Membrane swelling

ABSTRACT

Assembly pressure and membrane swelling induced by elevated temperature and humidity cause inhomogeneous compression and performance variation in proton exchange membrane (PEM) fuel cells. This research conducts a comprehensive analysis on the effects of assembly pressure and operating temperature and humidity on PEM fuel cell stack deformation, contact resistance, overall performance and current distribution by advancing a model previously developed by the authors. First, a finite element model (FEM) model is developed to simulate the stack deformation when assembly pressure, temperature and humidity fields are applied. Then a multi-physics simulation, including gas flow and diffusion, proton transport, and electron transport in a three-dimensional cell, is conduced. The modeling results reveal that elevated temperature and humidity enlarge gas diffusion layer (GDL) and membrane inhomogeneous deformation, increase contact pressure and reduce contact resistance due to the swelling and material property change of the GDL and membrane. When an assembly pressure is applied, the fuel cell overall performance is improved by increasing temperature and humidity. However, significant spatial variation of current distribution is observed at elevated temperature and humidity.

1. Introduction

Fuel cells are promising alternative power devices due to their high theoretical efficiency and environmental friendliness. In particular, proton exchange membrane (PEM) fuel cells are attractive for automotive and portable applications because of their low operating temperature, fast start-up, and low emissions. A PEM fuel cell stack consists of several single cells connected in series by bipolar plates (BPP) which provide reactants to the membrane electrode assembly (MEA). Assembly pressure can increase the overall electrical conductivity of the gas diffusion layer (GDL), improve contact resistance, and hence, reduce the electrical resistance losses inside a cell. Assembly pressure also determines the contact status and stack deformation especially that of the GDL, which is the most deformable component in a PEM fuel cell stack. Under the land of a bipolar plate, the GDL is compressed by the assembly force. Under the channel area, the GDL protrudes into the channel cavities. The thickness and porosity of the GDL are affected under compression; consequently, the mass, heat, and charge transfer properties are changed.

It is well recognized that the GDL can influence PEM fuel cell performance significantly [1]. However, most of PEM fuel cell performance models do not consider this GDL inhomogeneous compression and only limited research has been conducted to address this issue. Zhou et al. [2] developed a multi-physics model to investigate the effects of assembly pressure on PEM fuel cell performance by considering contact resistance and flow resistance. Sun et al. [3] assumed a GDL compression ratio and analyzed the influence of performance and current density distribution. Hottinen et al. [4] conducted a study on the effect of inhomogeneous compression of GDL on the mass and charge transfer in PEM fuel cells using experimentally obtained GDL parameters as a function of compression thickness. However, the room temperature and dry conditions were assumed in both modeling and experimental investigation on GDL deformation.

Room temperature and dry conditions do not reflect the real PEM fuel cell operating conditions since most fuel cells operate at elevated temperatures and 100% relative humidity (RH). Elevated temperature and high RH influence PEM fuel cell polarization losses in many ways including catalyst activity [5], membrane mechanical and electrical properties [6], and gas transport [7], etc. In addition, GDL and MEA deformation are also affected. Since the relative position between the top and bottom end plate of PEM fuel cell stack is fixed after assembly, the polymer membrane is spatially confined under the BPP (with the gas flow channels) and the porous carbon electrodes, as shown in Fig. 1. As the RH increases, membrane absorbs water, swells and pushes the electrodes. As a consequence, GDL will be further compressed under the land and the protrusion into channel increases due to the tendency of membrane swelling. This membrane swelling also changes the local contact forces due to the redistribution of the stress field in fuel cell stacks.

* Corresponding author. Tel.: +1 734 615 4315; fax: +1 734 647 7303.
E-mail address: jackhu@umich.edu (S.J. Hu).

0378-7753/$ – see front matter © 2009 Elsevier B.V. All rights reserved.
doi:10.1016/j.jpowsour.2009.01.085

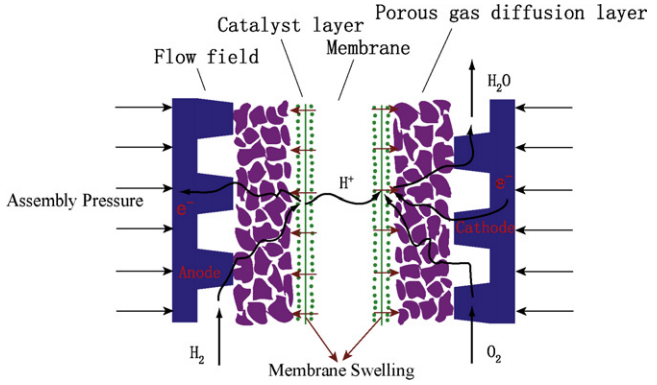

Fig. 1. Schematic of assembly and swelling in a PEM fuel cell.

Table 1
Simulation cases.

	Base case	Case 1	Case 2	Case 3
Pressure (MPa)	0	3	3	3
T (°C)	25	25	85	85
RH (%)	40	40	40	90

Table 2
Geometric and physical parameters for the structural deformation and mass transfer analysis.

Parameter	Value
BPP thickness (h_1)	2 mm
GDL thickness (h_2)	100 μm
Catalyst layer thickness (h_3)	20 μm
Membrane thickness (h_4)	50 μm
Channel height (h_5)	0.5 mm
Channel width (w_1)	1 mm
Land width (w_2)	1 mm
Channel length	5 mm
GDL initial porosity	0.6 [14]
Catalyst layer porosity	0.06 [14]
GDL electric conductivity	Uncompressed
In-plane	3.4×10^4 S m^{-1} [12]
Through-plane	1.4×10^2 S m^{-1} [12]
GDL permeability	1.76×10^{-11} m^2
Catalyst layer electronic conductivity	100 S m^{-1} [15]
Catalyst layer ionic conductivity	1.7 S m^{-1} [16]

This paper investigates the influence of operating conditions (temperature and RH) on stack deformation and contact resistance by improving the model previously developed by the authors [2] with respect to the effects of assembly pressure on fuel cell performance by incorporating temperature and RH effects with GDL deformation and contact resistance. Furthermore, this paper also investigates the current density distribution. During the operation of a PEM fuel cell, significant variation of the local current density exists across the plane of the cell. This causes sharp local temperature and stress gradient as well as degrading the efficiency of water management [8–10]. Current density distribution is also an important measure to evaluate fuel cell performance and durability. Current density distributions under various assembly pressure and operating conditions are investigated.

Table 4
Young's modulus (MPa) at various temperature and humidity for Nafion® 112 [6].

	H = 30%	H = 50%	H = 70%	H = 90%
T = 25 °C	197	192	132	121
T = 45 °C	161	137	103	70
T = 65 °C	148	117	92	63
T = 85 °C	121	89	59	46

A sequential approach is implemented in this study. A finite element model (FEM) is first developed to model the stack deformation under different levels of assembly pressure, temperature and RH. Component deformation, the change of material properties and local contact pressure are obtained from the FEM model. Then gas flow and diffusion, chemical reactions, ion and electron transport are modeled based the updated geometry and material properties. Contact resistance is also analyzed using the model. The impact of assembly pressure and operating conditions is evaluated by fuel cell performance and current density distributions.

2. Model description

A FEM based structural model is developed to simulate stack deformation under various assembly pressures, temperatures and RHs. Upon obtaining the deformed geometry and material properties of GDL and membrane, a computational fluid dynamic (CFD) based fuel cell performance model is developed to analyze the multi-component gas transport, chemical reactions, charge transfer and contact resistance based on the deformed GDL shape and modified GDL gas transport parameters. Specifically, the local contact force between BPP and GDL can be obtained. The contact resistance is then simulated based on Zhou et al. [11] and included in the multi-physics performance model to predict fuel cell performance.

Four different cases are modeled to analyze assembly pressure, temperature and relative humidity impacts as shown in Table 1.

2.1. Stack deformation model under elevated temperature and humidity

The model used in the current investigation is an extension of the model developed by Zhou et al. [2]. In the current work, temperature- and humidity-dependent properties of the membrane are incorporated in investigating stack deformation under various assembly pressures and operating conditions. The geometric parameters and physical properties of the components are listed in Tables 2–4, where the elastic constants, coefficients of swelling and thermal expansion of the component materials, are collected from various references [6,12,13].

A simple while representative 2D, single-channel, half-cell FEM model for the cathode side is built for stack deformation analysis. Such a simplification is pursued by taking advantage of the geometrical periodicity of the cell, and considering the fact that the length of gas channels is typically much larger (by ~100 times) than their cross-section dimensions, which justifies the plane-strain assumption.

The material properties for the graphite plates are set to those of commercial graphite material and for the carbon paper from TORAY® TGP-H-030. It is assumed that they do not swell in response to moisture. Especially for GDL, it is treated as nonlinear elastic

Table 3
Component material mechanical properties [6,12,13].

Component (material)	Elastic modulus (MPa)	Poisson's ratio	Coefficient of thermal expansion (α) (10^{-6} °C^{-1})	Swelling coefficient (β) (RH^{-1})
BPP (graphite)	10,000	0.25	5	Neglected
GDL (carbon paper)	Nonlinear elastic	0.25	−0.8	Neglected
Membrane (Nafion® 112)	Table 4	0.253	123	From Fig. 2

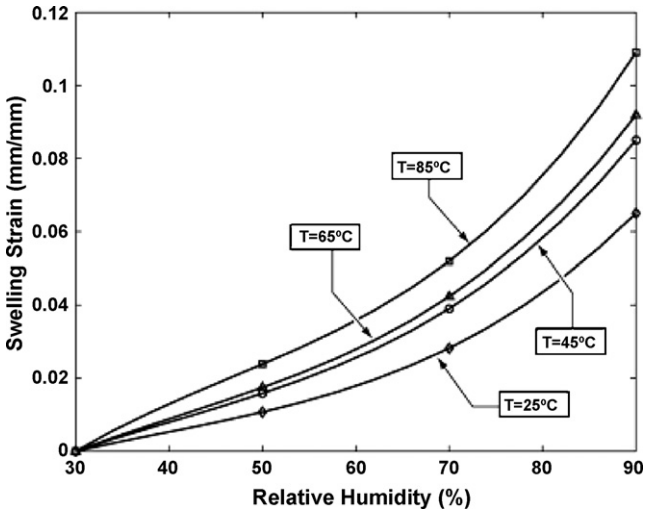

Fig. 2. Swelling expansion as a function of humidity and temperature for Nafion® 112 [6].

[12] since its material properties will settle down after the first few compression cycles. The compression curve for GDL is different from decompression curve. The compression strain–stress curve has been applied to calculate GDL deformation and contact resistance since in the model the assembly pressure on the stack is gradually increased in this analysis.

Linear elastic, perfectly plastic constitutive behavior with temperature- and humidity-dependent material properties is assumed for the membrane. Young's modulus and yield strength of the membrane are defined for four temperature and RH values based on experimental data for Nafion®112 from two literature. Even though a slight anisotropy in the material properties was observed experimentally [6], in this study we assume for simplicity that the material properties are isotropic (Fig. 2).

The model is built using the commercial FEM software ABAQUS. Four-node quadrilateral plane-strain elements (CPE4) are used to mesh the components, as shown in Fig. 3. The bottom membrane surface is fixed vertically (in *Y*-direction), and *X*-symmetry conditions are applied to the side vertical boundaries of all components. The component interfaces are bonded, with no-slip allowed. The analysis consists of two sequential steps, as described in the following.

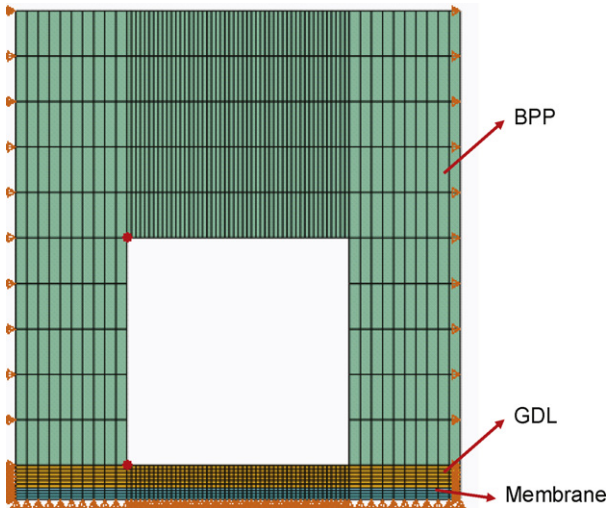

Fig. 3. Finite element model for stack deformation analysis.

2.1.1. Simulation of assembly-induced stack deformation

In the stack assembly, it is desirable to have a uniform assembly pressure in the BPP, even though the clamping load may be localized. As such, a uniform assembly pressure is assumed for the BPP. Under ambient conditions, i.e., 25 °C temperature and 40% RH, a series of assembly pressures of 0.3, 0.5, 0.7, 1.0, 2.0, 3.0, and 6.0 MPa are applied to the BPP top surface. The stack deformation is calculated under these assembly pressures.

2.1.2. Simulation of stack deformation due to swelling and thermal expansion

After the equilibrium state of the components is achieved under the applied pressure, the top surface of the BPP is fixed in the vertical direction at the deformed position. Temperature and RH of the whole stack are then raised to the desired levels, i.e., 85 °C and 40% RH, and 90% RH, under which the components expand and swell. Meanwhile, the increase of temperature and RH also changes the material properties, and leads to the redistribution of deformations in the whole stack under the constraint of end plates, or the constraint of BPP for the single-cell.

The total strain in the membrane due to moisture and temperature change is calculated based on the coefficients of swelling and thermal expansion. The swelling behavior is temperature-dependent, which makes the total strain calculation difficult to implement in FEM modeling since ABAQUS, which is similar to most of the commercial software package, can only simulate the expansion caused by the temperature field change. Thus, a new parameter, denoted as equivalent coefficient of expansion, α', is defined to overcome this challenge by combining the effects of swelling and thermal expansion. As the temperature and humidity are increased to T and RH, respectively, α' can be expressed as,

$$\alpha'(T,\ \mathrm{RH}) = \frac{[1+\alpha(T)\Delta T][1+\beta(\mathrm{RH},\ T)\Delta \mathrm{RH}(T)]-1}{\Delta T} \quad (1)$$

where α is the coefficient of thermal expansion (CTE), β is the coefficient of swelling expansion and calculated by data obtained from Fig. 2. ΔRH and ΔT are the changes of RH and temperature, respectively, from one state to another. When the humidity effect is neglected, i.e., $\beta(\mathrm{RH},T)=0$, $\alpha'(T,\mathrm{RH})=\alpha(T)$ and when the thermal expansion effect is neglected, i.e., $\alpha(T,\mathrm{RH})=0$, $\alpha'(T,\mathrm{RH})=\beta(\mathrm{RH},T)\Delta\mathrm{RH}(T)/\Delta T$.

The elevated temperature and humidity cases simulated are 85 °C and 40% RH, and 85 °C, 90% RH, which will be compared with the base case at 25 °C and 40% RH. Then the change of RH is converted to the equivalent of temperature change using Eq. (1). Through this way, the swelling and thermal expansion can be both considered in ABAQUS simulation.

Under the applied assembly pressure and the given temperature and RH, the volumetric strain of every element or the thickness of the GDL can be used to estimate its modified porosity. Based on the deformed configuration and the modified GDL porosity, mass transfer analysis is conducted.

It is assumed that the change in thickness under compression is due to change in volume of void space, not in volume of solid material. Thus, the porosity of the GDL can be calculated

$$\varepsilon' = \varepsilon_0 \frac{v' - v_{\mathrm{solid}}}{v_0 - v_{\mathrm{solid}}} \quad (2)$$

where ε_0 is the initial porosity of GDL, V_0 is the uncompressed volume and V' is the volume after compression. From the structure model above, the individual element volume can be exported so that local porosity is calculated accordingly.

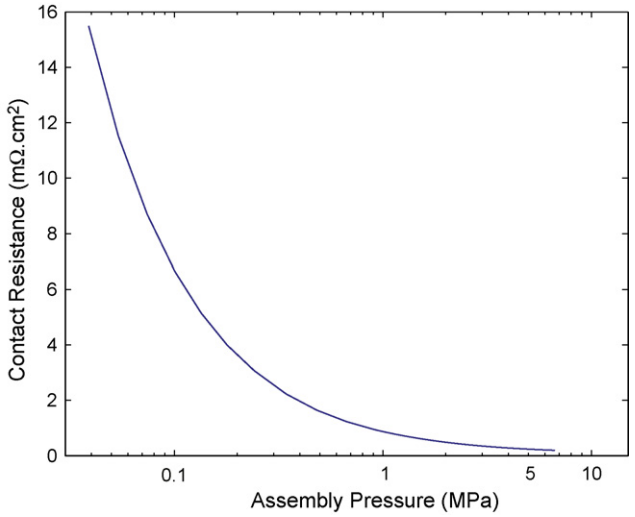

Fig. 4. Contact resistance vs. assembly pressure.

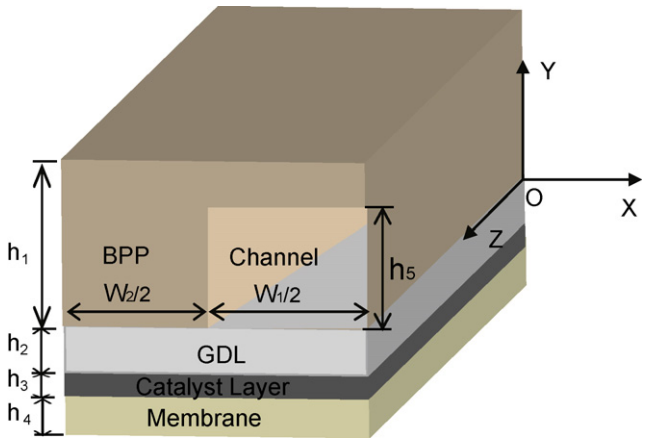

Fig. 5. Computational domain for the base case.

2.2. Contact resistance

Contact resistance constitutes a significant part of ohmic resistance in the fuel cell, and needs to be considered when evaluating fuel cell performance. A high contact resistance exists between the GDL and BPP due to the fact that the GDL is porous (60% to 80% porosity) and the surface of BPP engaging GDL is rough. Hence, current flow between BPP and GDL occurs only at sites where the BPP contacts GDL.

Assembly pressure affects contact resistance in PEM fuel cells. Contact resistance can be estimated based on surface roughness parameters of BPP and features of GDL structure. A detailed description of the model is presented in Zhou et al. [11].

BPP surface topology is simulated as randomly distributed asperities, and is based on measured surface roughness. The GDL is modeled as randomly distributed cylindrical fibers. Upon obtaining these two simulated surfaces, each contact spot is located according to relative positions. The total resistance and pressure are obtained by considering all contact spots as resistances in parallel and summing the results together.

In this study, the contact resistance between graphite BPP and carbon fiber paper GDL, the most common materials used in PEM fuel cells, is applied in the model. The surface roughness parameters obtained from the average values of several scans are: peak density D_{peak}=150 mm^{-1}, mean asperity summit radius R_1=3.26 μm, and variance of the summit height distribution σ_s=0.728 μm. The model predicted results of contact resistance change with assembly pressure is shown in Fig. 4.

Since the operating conditions will influence local contact force and GDL porosity, two crucial factors for determining contact resistance, the changes of contact resistance should be considered. The contact force and GDL porosity will be obtained from the structural model in Section 2.1.

2.3. PEM fuel cell performance analysis

A FEM computational fluid dynamics package, COMSOL Multiphysics®, is applied to solve the coupled nonlinear equations representing the physical phenomena of gas and charge transfer. Fig. 5 shows the model domain for the base case with no assembly pressure, 25 °C temperature and 40% RH. The 3D model domain consists of a conventional gas channel, cathode GDL, catalyst layer (CL), membrane, and anode electrode interface. Because of the symmetrical characteristic of the structure, only half the width of the shoulder and channel is analyzed to reduce computational time.

There exist coupled gas mass transfer and charge transfer in PEM fuel cell stacks. In the BPP channel, multi-component gases consist of N_2, O_2 and H_2O. Gas flow and components in BPP channel is dependant on diffusion in GDL and oxygen consumption rate at the catalyst layer. The gas flow is modeled in combination with diffusion and convective transport. In the GDL and CL, N_2, O_2 and H_2O transport is driven by diffusion mechanism. Three sets of Navier–Stroke equations are used to model the incompressible gas flow of N_2, O_2 and H_2O in channels and another three sets of Maxwell–Stefan equations are used to simulated multi-component diffusion and convection in channels and gas distribution layers. The velocity of gases through GDL is modeled as Darcy's flow since there exists pressure difference across the GDL. The rate of O_2 consumption and H_2O production are determined by coupled effects of gas transfer rate and charge transfer processes. Those coupled equations will be solved simultaneously to obtain the steady state of gas flow, diffusion and chemical reactions.

Charge balance in the solid phase (GDL, membrane and CL) is taken into account in this model, including the ion transport in CL and membrane and electron transport in GDL and CL. In GDL, due to no chemical reactions, the electronic charge is conserved. Within the CL, electrons are consumed by the O_2 reduction reaction and the O_2 consumption rate varies across the CL. The gradient of the electronic current is proportional to the oxygen consumption rate. The contact resistance between GDL and the land of BPP is taken into account by modeling the boundary as a thin layer. The electric conductivity and thickness of the boundary layer are calculated so that its total resistance corresponded to the contact resistance values obtained from the mechanical deformation model and contact resistance simulation in Section 2.2. Ion transfer only takes place in CL and membrane. Ions are consumed at the CL due to chemical reactions. The ion transfer is conserved in the membrane domain.

For boundary conditions, gas mixture is assumed to enter the channel normal to the inlet cross-section. All walls in the channel have no-slip boundary conditions. The mass and momentum transport boundary conditions between the BPP shoulders and the GDL are all insulated. At the interface between GDL and CL, it is assumed that no contact resistance exists. The electronic current and the fluxes of N_2, O_2 and H_2O in the *Y*-direction are continuous. The flux of protons is set to zero because there is no ionic phase in the GDL. At the boundary between the CL and the membrane, the fluxes of N_2, O_2 and H_2O, and electronic current in the *Y*-direction are set to zero while the ionic current are continuous. The anode is assumed to be an interface, and the ionic potential is approximately zero at the interface between the anode CL and the membrane based on

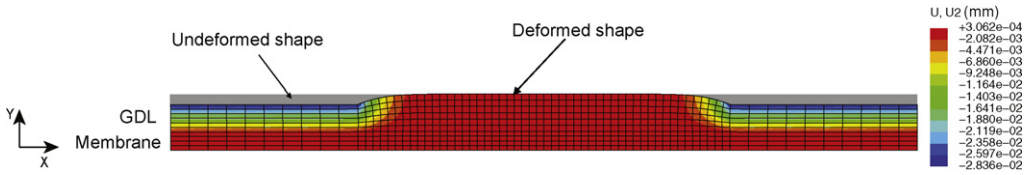

Fig. 6. Model predicted contour of displacement at *Y*-direction under 3 MPa assembly pressure.

the assumption that the hydrogen oxidation reaction rate is so fast that the anodic overpotential is negligible [14]. All other boundaries are assumed to be insulated due to symmetry.

Consistent with traditional fuel cell models [17,18], the model is assumed to be steady state, isothermal and isobaric. Another assumption is that single-phase water transport. Water exists only in the gas phase. The existence of liquid water is taken into account by using effective porosity as the initial porosity for GDL, which may be significantly smaller than the raw material because of possible flooding by liquid water.

The geometric and physical properties of the components are listed in Table 2. The electrical conductivity in the CL is assumed to be 100 S m^{-1} for all the cases. For the GDL, the electrical conductivity is anisotropic. The relationship between in-plane σ_{xz} vs. the through-plane conductivity σ_y follows the relationship related to channel geometry and thickness of GDL [12]:

$$\frac{\sigma_{xz}}{\sigma_y} = \frac{(w_1 + w_2)w_1}{8h_2^2} \tag{3}$$

A wide range of GDL conductivity values have been employed in various PEM fuel cell models. In this study, based on the experimental data from Mathias et al. [12], through-plane conductivity for Toray carbon fiber paper is 1369 S m^{-1} in the base case (no compression). The in-plane conductivity of carbon fiber paper is over an order of magnitude larger than the through-plane value. And the channel/land geometry imposes stricter requirements on the through-plane conductivity.

Both the in-plane and through-plane conductivities increase monotonically with increase of assembly pressure, with the change in through-plane conductivity especially significant. The change of GDL conductivities follows the relationship obtained experimentally by [4], as shown in Table 5.

Some parameters change with temperature and humidity. The open circuit potential E^0 for the overall reaction is calculated as [19]:

$$E^0 = 0.2329 + 0.0025T \tag{4}$$

The binary diffusivities D_{ij}, obtained experimentally at atmospheric pressure, are scaled with the temperature and pressure according to Cussler [20].

$$D_{ij} = D_{ij}(T_0, p_0)\frac{p}{p_0}\left(\frac{T}{T_0}\right)^{1.5} \tag{5}$$

The membrane conductivity depends on RH. The following relationship between ionic conductivity σ (in the unit of S cm^{-1}) and RH obtained from curve fitting the experimental data is employed [21].

$$\sigma = 1.3 \times 10^{-7} \exp(14\,\mathrm{RH}^{0.2}) \tag{6}$$

Table 5
GDL electrical conductivities.

GDL electrical conductivity	Base case (uncompressed)	3 MPa
In-plane	3.4×10^4 S m^{-1} [12]	3.43×10^4 S m^{-1}
Through-plane	1.4×10^2 S m^{-1} [12]	1.65×10^2 S m^{-1}

Using deformed geometry and parameters for each case, the relationship between cell voltage and current density can be obtained by setting the potential of cathode current collector to cell voltage. COMSOL Multi-physics® is used to solve the coupled nonlinear equations for gas and charge transfer. Details of the model, geometry meshing and solver settings were consistent with previous model [1].

3. Results and discussion

3.1. GDL and membrane deformation

The membrane and GDL are pre-stressed due to the applied clamping as explained previously The displacement under 3 MPa of assembly pressure (25 °C temperature and 40% RH) is calculated and shown in Fig. 6. Compared to GDL and membrane, BPP is a very stiff material and has very small deformation. Fig. 6 only shows the bottom parts of Fig. 3, including GDL and membrane. The GDL is deformed severely under the land, but it is almost unchanged under the channel. The membrane has very little deformation because it has larger Young's modulus compared to that of GDL.

Fig. 7 shows the deformation of GDL and membrane when temperature and RH change under the same assembly pressure (3 MPa). When temperature and RH increase, swelling of membrane pushes GDL more into the channel cavity and the contact surface between GDL and membrane becomes curved. But the thickness of GDL under the channel almost remains the same and that the total change from the original uncompressed volume remains small.

BPP, GDL and membrane all have thermal expansion to some extent, although the thermal expansion coefficients for GDL and BPP are very small. For membrane, the special characteristic is that it also expands with respect to humidity. Therefore, the total strain in the membrane due to change in moisture and temperature is calculated from the coefficients of swelling and thermal expansion. When temperature increases to 85 °C, there is a slight variation of

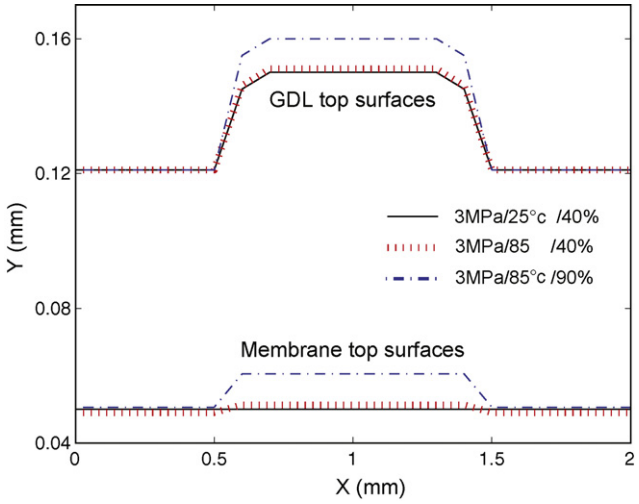

Fig. 7. Deformed shape of GDL and membrane at various conditions.

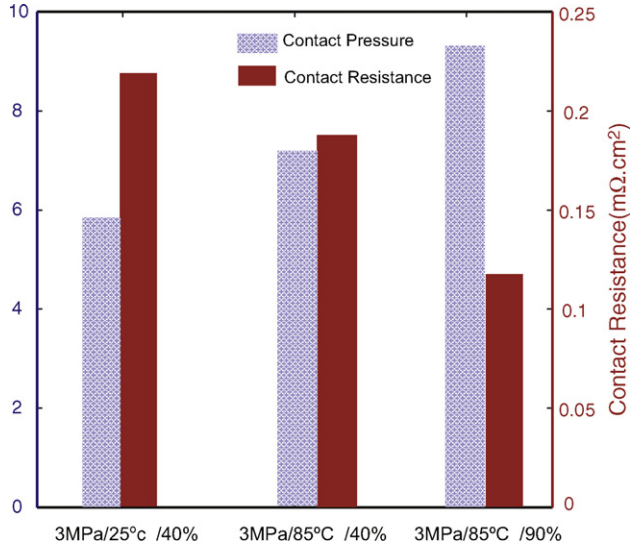

Fig. 8. Contact pressure and contact resistance at various operation conditions.

the GDL and membrane deformation. It is mainly due to the fact that the temperature induced strains for both GDL and membrane are very small even though the Young's modulus of membrane drops by about 40%. Swelling expansion coefficient due to moisture absorption is defined as the relative change in length per 1% RH change. When RH increases to 90%, membrane becomes softer since its Young's modulus drops from 197 MPa to 46 MPa. Whereas, swelling induced strain for membrane is significant.

Fig. 8 shows the change of contact pressure and contact resistance. The contact pressure at 3 MPa/25 °C/40%RH condition is 5.78 MPa and contact resistance is 0.22 mΩ cm^2. When the temperature increases to 85 °C, the contact pressure goes up to 7.2 MPa and contact resistance decreases to 0.198 mΩ cm^2. When RH further increases from 40% to 90% at 85 °C, the contact pressure increases to 9.3 MPa and contact resistance is 0.12 mΩ cm^2. That is due to the re distribution of the stress field in the stack. Since the relative location between upper surface of BPP and lower surface of membrane is fixed after assembly, the resulting displacement at the upper boundary from the previous step is fixed throughout the analysis. The internal forces have to be redistributed to accommodate additional loading. Hence the contact force is changed when fuel cell operating conditions change. When membrane swells, the contact force becomes larger. The contact force between BPP shoulder and GDL determines the contact resistance in between. The change of contact resistance should be considered when evaluating fuel cell overall performance.

When the stack is not well assembled, the contact resistance could be very high, ranging up to a few hundreds mΩ cm^2 in a fuel cell stack [22]. A reasonable value of 20 mΩ cm^2 is assumed in the base case model [23]. The contact resistance under 3 MPa assembly pressure and various operating conditions are significantly smaller due to higher electrical conductivity and smoother contacting surfaces used in the simulation.

3.2. Performance model

3.2.1. Polarization curves

The polarization curves are obtained by solving the average current density for different values of cell voltage. Fig. 9 shows the polarization curves for the four cases. In brief, assembly pressure causes performance decrease but higher temperature and RH increase the polarization curves over the entire operating range of the cell.

It is observed that under the assembly pressure of 3 MPa, the performance decreases which is consistent with previous findings [1]. Such a performance deterioration is mainly due to the fact that compression causes a decrease of GDL porosity which then imposes more resistance to gas flow, even though compression reduces contact resistance. There are no significant differences between the compression case (3 MPa/25 °C/40%RH) and the base case at the cell voltage level, indicating that the overall cell performance is not significantly affected by the assembly pressure at 3 MPa for this set of component geometry and material properties.

When temperature increases from 25 °C to 85 °C, the performance curve has a moderate increase. This is due to the total effects of contact resistance reduction, GDL protrusion and the change of some kinetic parameters. Contact resistance reduction leads to the decrease of ohmic voltage loss. GDL deformation reduces gas flow area and through-plane thickness, which can facilitate the gas flow therefore reduces flow resistance. Also, the diffusion characteristics of gas mixture and kinetic parameters increase with temperature, which benefit for gas diffusion, and result in the decrease of the cathode activation overpotential with temperature.

When RH goes to 90%, the performance curve has a more significant increase. When RH increases, the ionic conductivity the membrane increases, so that the overpotential is decreased. In terms of cell performance, this is desirable because lower overpotentials result in higher cell voltage. Also the change of RH has more impacts on contact pressure and contact resistance between BPP and GDL, as shown in Fig. 8. When RH increases from 40% to 90%, the contact resistance drops more. This is one of the contributing factors for the performance increase. In addition, GDL is more protruded into BPP channel due to swelling and the change of material properties, and the change of porosity and flow channel area reduction are beneficial to gas flow and diffusion, which will in turn improve performance. All those effects integrate together to yield the performance better with higher temperature and humidity.

3.2.2. Current production rate in CL along the channel length direction

Fig. 10(a) and (b) presents the current production rate and variation at the interface between GDL and catalyst layer along the channel direction for three cases when the cell voltage is 0.5 V. When the assembly pressure, elevated temperature and RH are all taken into account, there is a significant change of the current production rate at this interface.

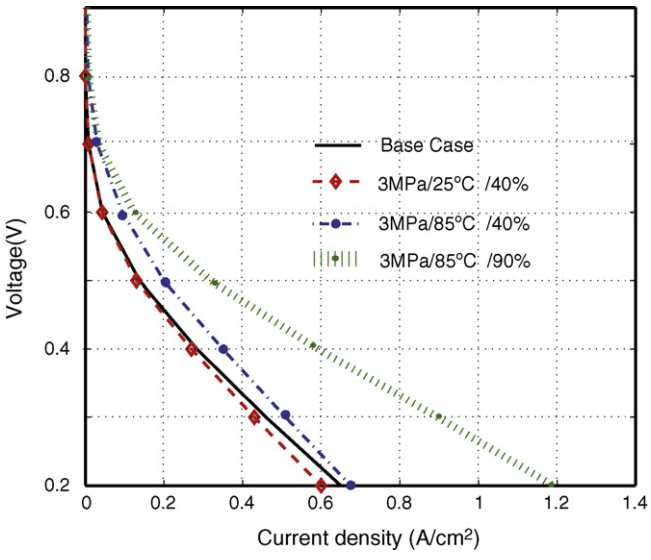

Fig. 9. Polarization curves for various cases.

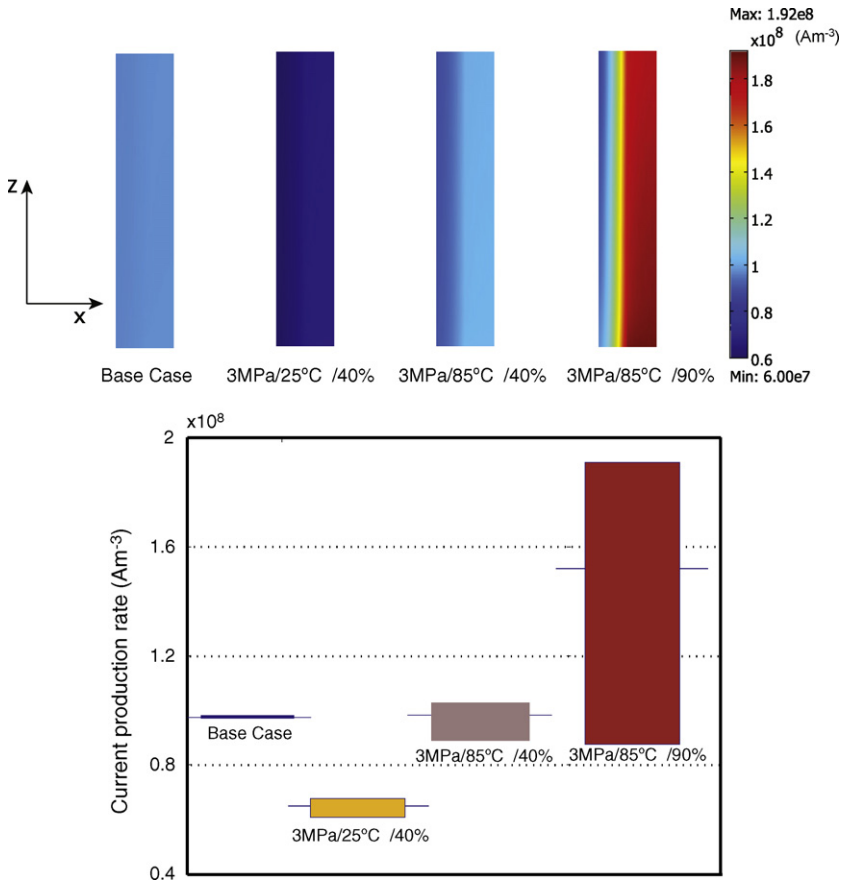

Fig. 10. Current production rate profiles at the interface between CL and GDL for different cases at 0.5 V.

When an assembly pressure of 3 MPa is applied, the average current density of the case at 3 MPa/25 °C/40% is lower than the base case (0 MPa/25 °C/40%) since assembly pressure causes performance decrease. The current production rate starts to have some variations along the channel length direction at this interface. At the base case, the current production rate only has 1.7% variation compared with the average value over the whole surface. At the compression case (3 MPa/25 °C/40%), the current production rate variation is increased to 10%. This is due to the fact that assembly pressure induces large unevenness of GDL porosity. GDL porosity is approximately 0.3 under the BPP land while 0.6 under the BPP channel for the compression case. This vari-

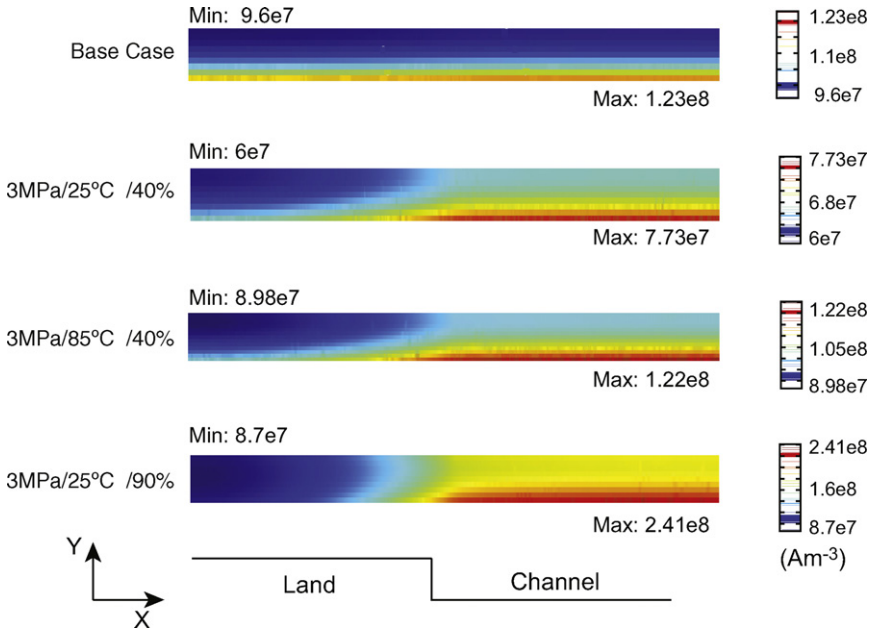

Fig. 11. Current production rate profiles in the CL for different cases at 0.5 V.

ation in GDL porosity causes the variation in current production rate.

When temperature rises to 85 °C, the average current production rate is higher since the voltage output increases with temperature, while the variation of current production rate increases to 15%. Temperature increase causes more inhomogeneous compression, which in turn causes more current generation under the channel and less current generation under the land.

When RH increases to 90%, the average current production rate is substantially increased since the voltage output increases greatly at higher RH because of higher membrane conductivity and smaller contact resistance. Meanwhile, the current production rate variation is also increased to 68%. A notable portion of current is generated mostly under the channel and the current production rate is reduced under the BPP land. That is attributed by the fact that the inhomogeneous compression is much more severe when RH increases as shown in Fig. 7. Thus GDL porosity unevenness becomes more significant. It is more difficult for the gases to transport into the GDL under the land; hence the GDL under the land is in the starvation of reactant gases and generates less current.

3.2.3. Current production rate in CL along the thickness direction

Fig. 11 shows the distributions of current production rate in the thickness direction of the CL at the cell voltage of 0.5 V and $Z = 2$ mm. The same trends as in Fig. 10 can be observed. Both compression and elevated temperature and RH cause significant variation along the CL thickness and width direction. Less current is produced under the land area, because of the reduced oxygen diffusion in compressed region. More current is generated under the channel area which is caused by the combined effects including the dependence of diffusion parameters and kinetic parameters on temperature and RH, GDL protrusion and porosity variation. As shown in Fig. 7, GDL is expanded under the channel area so that the porosity is increased. Thus the gas transfer is facilitated and more current is generated.

4. Conclusions

In this paper we presented a comprehensive analysis of the influence of elevated temperature and relative humidity on fuel cell stack deformation, contact resistance and performance. Elevated temperature and humidity, especially humidity, caused severe GDL protrusion and stress-redistribution, which lead to the reduction of contact resistance. Even though elevated temperature and RH improved fuel cell performance, significant variation of current production rate was observed along all directions in the cell when assembly pressure was applied and temperature and RH were increased close to the operation conditions. The stack would be more prone to degradation with such a significant variation. One of the future research topics is the assembly optimization at various operating conditions to improve performance as well as mitigate the current variation.

References

[1] J. Ge, A. Higier, H. Liu, J. Power Sources 159 (2006) 922–927.
[2] Y. Zhou, G. Lin, A. J. Shih, S. J. Hu, ASME J. Fuel Cell Sci. Technol., in press.
[3] W. Sun, B. Peppley, K. Karana, J. Power Sources 144 (2005) 42–53.
[4] T. Hottinen, O. Himanen, S. Karvonen, I. Nitta, J. Power Sources 171 (2007) 113–121.
[5] K.C. Neyerlin, H.A. Gasteiger, C.K. Mittelsteadt, J. Jorne, W. Gu, J. Electrochem. Soc. 152 (2005) A1073–A1080.
[6] Y. Tang, A. Karlsson, M. Santare, M. Gilbert, S. Cleghorn, W. Johnson, Mater. Sci. Eng A 425 (2006) 297–304.
[7] M. Coppo, N.P. Siegel, M.R. Spakovsky, J. Power Sources 159 (2006) 560–569.
[8] Y. Zhang, A. Mawardi, R. Pitchumani, ASME J. Fuel Cell Sci. Technol. 3 (2006) 464–476.
[9] S. Um, C.Y. Wang, K.S. Chen, J. Electrochem. Soc. 147 (2000) 4485–4493.
[10] V. Gurau, H. Liu, S. Kakac, AIChE J. 44 (1998) 2410–2422.
[11] Y. Zhou, G. Lin, A.J. Shih, S.J. Hu, J. Power Sources 163 (2007) 777–783.
[12] M. Mathias, J. Roth, J. Fleming, W. Lehnert, in: W. Vielstich, A. Lamm, H.A. Gasteiger (Eds.), Handbook of Fuel Cells–Fundamentals, Technology and Applications, V3: Fuel Cell Technology and Application, Wiley, 2003, pp. 517–538.
[13] A. Kusoglu, M.A. Karlsson, M.H. Santare, S. Cleghorn, W.B. Johnson, J. Power Sources 161 (2006) 987–996.
[14] G. Lin, T.V. Nguyen, J. Electrochem. Soc. 153 (2006) A372–A382.
[15] A. Fischer, J. Jindraz, H. Wendt, J. Appl. Electrochem. 28 (1998) 277–282.
[16] D. Bevers, M.W. Wohr, J. of Appl. Electrochem. 27 (1997) 1254–1264.
[17] T. Berning, D. Lu, N. Djilali, J. Power Sources 106 (2002) 284–294.
[18] D.M. Bernardi, M.W. Verbrugge, AICHE J. 37 (1991) 1151–1163.
[19] A. Parthasarathy, S. Srinivasan, A.J. Appleby, J. Electrochem. Soc. 139 (1992) 2530–2537.
[20] E.L. Cussler, Diffusion-Mass Transfer in Fluid Systems, Cambridge University Pressure, Cambridge, UK, 1984.
[21] C. Yang, S. Srinivasan, A.B. Bocarsly, S. Tulyani, J.B. Benziger, J. Membr. Sci. 237 (2004) 145–161.
[22] G. Inoue, Y. Matsukuma, M. Minemoto, J. Power Sources 157 (2006) 136–152.
[23] S. Escribanoa, J. Blachota, J. Ethèvea, A. Morina, R. Mosdaleb, J. Power Sources 156 (2006) 8–13.